npj | Flexible Electronics

www.nature.com/npjflexelectron

ARTICLE OPEN

Check for updates

Aerosol jet printed capacitive strain gauge for soft structural materials

Kiyo T. Fujimoto[1,2,3], Jennifer K. Watkins[1,2,4], Timothy Phero[1,2], Doug Litteken[5], Kevin Tsai[3], Takoda Bingham[6], Kshama Lakshmi Ranganatha[7], Benjamin C. Johnson[7], Zhangxian Deng[6], Brian Jaques[1,2] and David Estrada[1,2]✉

Soft structural textiles, or softgoods, are used within the space industry for inflatable habitats, parachutes and decelerator systems. Evaluating the safety and structural integrity of these systems occurs through structural health monitoring systems (SHM), which integrate non-invasive/non-destructive testing methods to detect, diagnose, and locate damage. Strain/load monitoring of these systems is limited while utilizing traditional strain gauges as these gauges are typically stiff, operate at low temperatures, and fail when subjected to high strain that is a result of high loading classifying them as unsuitable for SHM of soft structural textiles. For this work, a capacitance based strain gauge (CSG) was fabricated via aerosol jet printing (AJP) using silver nanoparticle ink on a flexible polymer substrate. Printed strain gauges were then compared to a commercially available high elongation resistance-based strain gauge (HE-RSG) for their ability to monitor strained Kevlar straps having a 26.7 kN (6 klbf) load. Dynamic, static and cyclic loads were used to characterize both types of strain monitoring devices. Printed CSGs demonstrated superior performance for high elongation strain measurements when compared to commonly used HE-RSGs, and were observed to operate with a gauge factor of 5.2 when the electrode arrangement was perpendicular to the direction of strain.

npj Flexible Electronics (2020)4:32 ; https://doi.org/10.1038/s41528-020-00095-4

INTRODUCTION

Soft structural textiles, also known as softgoods, that are lightweight while also exhibiting high strength are of particular interest to the space industry for inflatable habitats, parachutes and decelerator systems. The advantages of these technical textiles over traditional structural materials such as metal alloys and rigid composites are found in the significant mass and volume savings that they provide[1]. Benefits aside, complexities emerge from the need to incorporate non-destructive/non-invasive testing methods for structural health monitoring (SHM), which requires monitoring systems capable of measuring very high rates of strain[2]. SHM systems for inflatable habitats, parachutes and decelerating systems are used to ensure the safety of crewmembers, aim to establish an emergency notification system, and enable smart entry, descent, and landing (EDL) operations. Ideally, SHM systems for these applications would provide continuous monitoring of strain/load to detect, diagnose and locate damage in real time for continuous monitoring and also after incident[3].

Detecting mechanical deformations is achieved with a variety of sensing mechanisms such as capacitance, resistance or piezoelectric properties. However, the most widely used strain sensing devices, are resistance-based strain gauges (RSG)[4]. Traditionally, strain gauges are intended for use with metals, they employ relatively stiff substrates, operate most effectively at room temperature before corrections must be incorporated, experience strains under 5%, display hysteresis in long-term testing, and undergo mechanical failure at higher strains[2–5]. When considering soft structural materials strain gauges must be capable of withstanding high rates of strain (5–50%) associated with materials being under high load, but the inherent stiffness of traditional strain gauges results in device failure, and classifies them as unsuitable for the inspection of soft structural materials[3,5]. Additional limitations of the more popular RSGs are found in the dependence of resistivity upon operating temperature and applied strain[4,6,7]. Dependencies such as this result in a non-linear strain response and device hysteresis caused by variable sensitivity as the gauge factor does not remain constant during testing[6–8]. Finally, the fabrication of traditional strain sensors involves complex preparation processes resulting in high fabrication cost and material waste, which can limit their application and development. Hence, developing strain sensing methods for soft structural materials requires the ability to fabricate devices having high flexibility and a robustness that enables them to withstand harsh environments to include high strain and high temperatures.

Capacitance based strain gauges (CSGs) provide a robust sensing mechanism capable of addressing the performance issues associated with resistivity hysteresis of RSGs. CSGs are largely dependent on geometry changes between the electrodes and the dielectric layer which typically do not suffer permanent plastic deformation during cyclical testing[2,9]. These devices, in general, include parallel-plate capacitors or an interdigitated electrode design[4,5,10,11]. CSGs can be used for many of the same applications as RSGs, and typically display higher gauge factors of 15–30, while also having reduced sensitivity to noise and temperature[2]. Currently, commercial CSGs are available, and typically consist of a parallel plate design restricting strain measurements to those that are perpendicular to the gauge direction, are limited in the geometries they can monitor, or require bulky electromechanical devices for mechanical attachment[2,12]. These issues can be overcome by using CSGs having an interdigitated electrode design[13,24]. Interdigitated electrodes preserve the advantages associated with CSGs vs RSGs in harsh environments, while also

[1]Center for Advanced Energy Studies, Boise State University, Idaho Falls, ID, USA. [2]Micron School of Materials Science and Engineering, Boise State University, Boise, ID, USA. [3]Measurement Sciences Department, Idaho National Laboratory, Idaho Falls, ID, USA. [4]Department of Advanced Fuel Manufacturing and Development, Idaho National Laboratory, Idaho Falls, ID, USA. [5]NASA Johnson Space Center, Houston, TX, USA. [6]Department of Mechanical and Biomedical Engineering, Boise State University, Boise, ID, USA. [7]Department of Electrical and Computer Engineering, Boise State University, Boise, ID, USA. ✉email: daveestrada@boisestate.edu

Published in partnership with Nanjing Tech University

npj nature partner journals

providing a vehicle by which CSGs can integrate directly onto structural components. Previous testing has been conducted on Kevlar webbing with flexible strain gauges and it was concluded that CSGs performed better than RSGs in dynamic and long term loading conditions similar to those that were investigated within this work[3]. Finally, using capacitance as the sensing mechanism makes the sensor more suitable for applications where wireless strain sensor measurements are required[10,14]. This would be tremendously advantageous for SHM during smart EDL operations.

Introducing the flexibility needed for SHM of soft structural materials can be achieved by making use of recent advances in additive manufacturing for printed and flexible electronics. Additive manufacturing techniques such as aerosol jet printing (AJP) are relatively simple and low-cost manufacturing processes that can be used to fabricate flexible CSGs where typical substrates employed for flexible applications include polyimide, polyethylene terephthalate and polydimethylsiloxane[2,15–18]. Printed electronics involve the use of a functional material in the form of a nanoparticle suspension, or ink, that is then deposited onto a flexible polymer backing. After deposition, the solvent and dispersing/capping agents are removed to produce a functional device, which is then attached to either the users clothing or skin. This cross-cutting technology demonstrates significant potential for SHM of soft structural materials as the functionality of these devices are dependent upon their high flexibility, long durability, fast response, fast recovery time and high sensitivity to strain.

The AJP technology is a non-contact deposition based on the atomization of inks to form a fine mist or aerosol that is deposited on a substrate. The aerosol jet process eliminates many of the limitations associated with conventional fabrication methods by introducing the ability to print with a wide range of materials such as metal nanoparticles, carbon nanomaterial, functional ceramics, semiconductors, biological molecules and other functional materials as inks can range from 1 to 2500 cP[15,19–23]. In addition, device designs are no longer material or geometry limited as AJP introduces the ability to print on a variety of substrates/surfaces, and provides a wide range of feature sizes that span 10 µm to 5 mm[24–27]. With the ability to achieve higher print resolutions, AJP has the potential to enhance device sensitivity by maximizing the design space of structural health monitoring systems, and provides a low-cost option for sensor fabrication[28–30].

In this work we report, on the response of aerosol jet printed flexible CSGs having an interdigitated electrode design (adapted from Hu et al.) targeted for use on soft structural materials[31]. The strain response of these printed gauges was then compared to that of commercially available high elongation resistance-based foil strain gauges (HE-RSG). This comparison was used to evaluate the benefits of utilizing the advanced manufacturing technique of AJP to fabricate a robust and flexible strain gauge, while also serving to validate the advantages of a capacitive sensor for measuring the strain of soft structural materials. Flexible CSGs were fabricated via AJP using silver nanoparticle ink and a flexible polymer substrate to monitor military grade Kevlar webbing under high load as this material is typically used in EDL operations and inflatable habitat structures. However, the focus of this work was towards inflatable habitats. Dynamic, static, and cyclic loads were used to characterize both types of strain monitoring devices. Printed CSGs demonstrated superior performance for high elongation strain measurements of Kevlar webbing when under high load when compared to commonly used HE-RSGs, and were observed to operate with a gauge factor of 5.2 when an electrode arrangement perpendicular to the direction of strain was used.

RESULTS

Printed CSG design

Military grade Kevlar webbing is used for the construction of inflatable habitats and parachutes, and the ability to measure the strain experienced by these structures is a challenge for NASA[3]. To produce a capacitive strain gauge, an interdigitated structure was employed, which operates in a similar manner to having multiple parallel plate capacitors in series. A schematic representation of the device layout can be found in Fig. 1a, and an optical image of the actual printed sensor in Fig. 1b. Capacitance was a result of an interdigitated structure spanning 3.6 cm and 1.6 cm with 50 digit pairs or 100 total electrodes. These specific design parameters were chosen to maximize both the theoretical capacitance and the sensing area. Additionally, size limitations were associated with the capabilities of the aerosol jet printing technology, and the 2.54 cm wide Kevlar webbing. Silver epoxy was used to attach copper wire leads to the device, and poly methyl methacrylate (PMMA), having a dielectric constant of 5.70, was used both as a protective layer and as the dielectric between the electrodes to enhance the device capacitance over what could be achieved if air served the same function[20]. Finally, Kapton (FPC 5 mil, 125 µm) was selected as the flexible substrate as it is capable of withstanding elongation that is significantly higher than the maximum elongation of the Kevlar straps when subjected to maximum loading capacity[32]. The CSGs were attached to the Kevlar straps using All-Purpose Barge Cement (APBC).

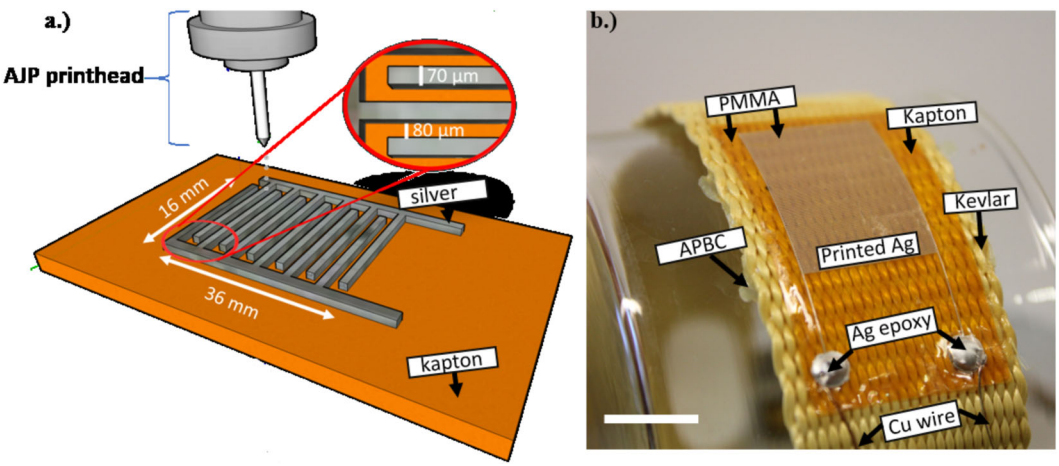

Fig. 1 Design of printed flexible interdigitated electrode capacitive strain gauge. a Schematic of the sensor configuration having an interdigitated electrode structure containing 50 digit pairs, **b** Optical image of capacitive strain gauge on Kapton substrate attached to Kevlar strap (scale bar represents 1 cm).

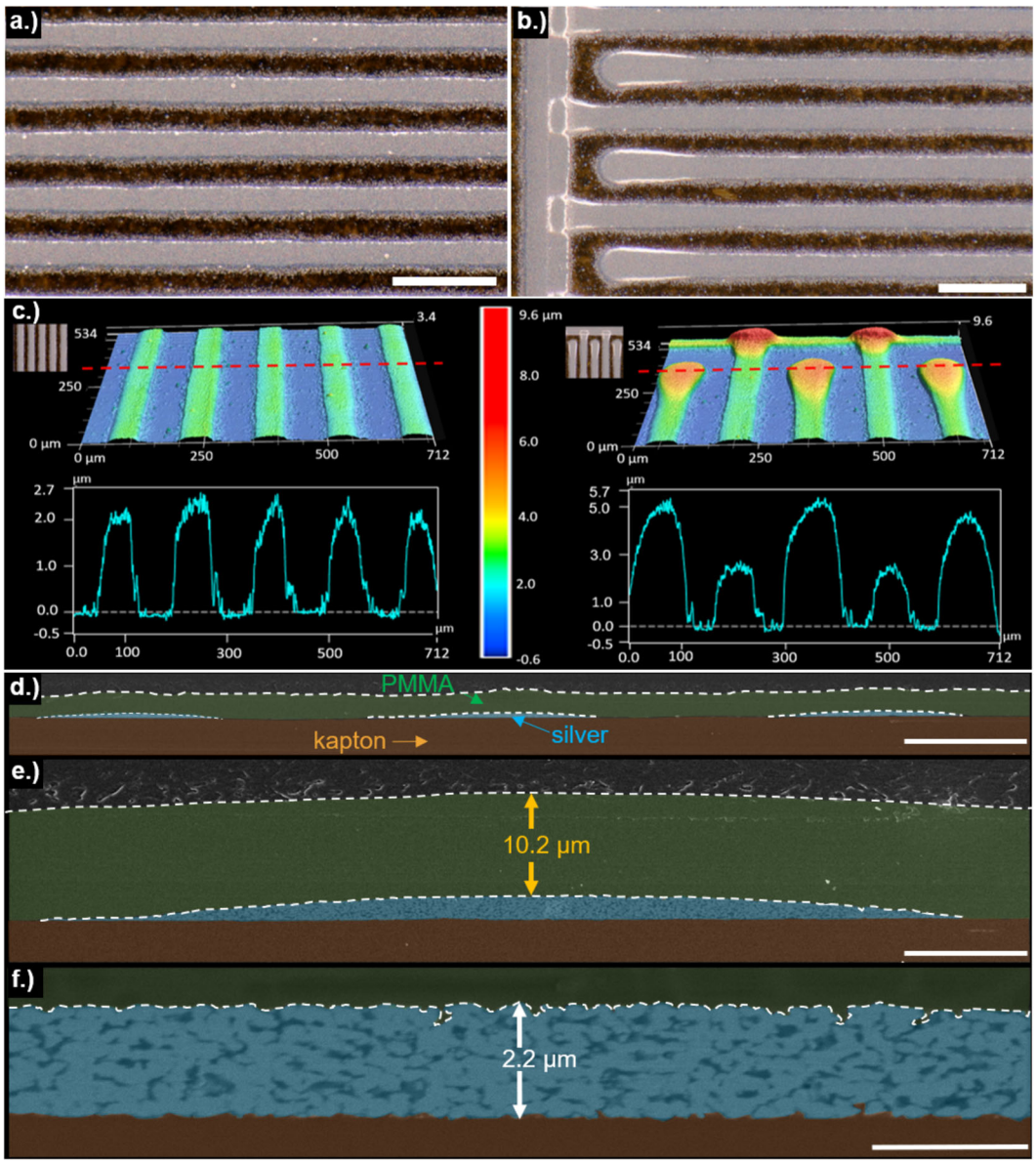

Fig. 2 Micrographs depicting the morphology of silver lines deposited with aerosol jet printing. a and **b** Optical microscope images of silver strain gauge on polyimide substrate (Scale bar represents 250 µm), and the **c** optical profilometry of AJP deposited silver electrodes on polyimide. Cross-sectional scanning electron microscopy characterization to show **d** silver electrodes representative of AJP deposited strain gauges (scale bar represents 50 µm), **e** PMMA dielectric thickness (scale bar represents 10 µm) and **f** printed silver thickness (scale bar represents 2.5 µm).

In Fig. 2, representative higher magnification images are shown of the digits (Fig. 2a center and Fig. 2b ends) along with their respective height profiles (Fig. 2c). As depicted, the electrode morphology varies due to the formation of a bulb-like structure at the electrode ends where variation is seen in both height and width. Rahman et al. reported the formation of a similar feature at the ends of their printed electrodes while also stating that this change in morphology could be controlled by increasing the printer's shutter speed while using Clariant Prelect TPS 50G2 with the ultrasonic atomizer[33].

For this study, devices were printed using the pneumatic atomizer for a silver nanoparticle based ink, PVNanoCell Sicrys^{TM} 160PM-116, known for having excellent adhesive properties with a variety of substrates, and near bulk resistivity ($10^{-6}\,\Omega\,cm$). During the printing process the shutter speed is ultimately controlled by the "rapid" process speed, which controls the speed at which the printer platen moves between depositions. For the fabrication of the CSGs the maximum rapid speed was used, but the formation of the bulb resulted despite modifications to other print parameters such as atomizer, exhaust, and sheath flow rates. This demonstrates that the quality of the print and ultimately the device is dependent upon the ink and atomization process being used.

Printed CSG structure

To further characterize the structure of the printed CSG, cross-sectional SEM was performed to investigate both the quality of the printed CSG and that of the dielectric layer (Fig. 2d). Preparing the sample for imaging required the device to be mounted in Quickstick 135 mounting wax prior to slicing with a microtome, and finally the cross-section was carbon coated to minimize surface charging while imaging. A top-down view of the overspray is provided in Fig. 2a, and a cross-section view is presented in Fig.

2e with the overspray creating a "tail" on either end of the digit. From Fig. 2e, the overspray is more pronounced on the left side of the digit, which indicates that N_2 flow was not symmetrical through the nozzle and/or the virtual impactor. The PMMA layer was uniform having a thickness of 10.2 ± 0.1 µm demonstrating that the drop cast method is an effective way of encapsulating the digits, which is crucial for maximizing the measured capacitance of CSG devices. The maximum thickness of the digit was 2.7 ± 0.1 µm, which is in good agreement with results obtained from stylus profilometry (2.2 ± 0.5 µm). The cross-section profile shows the porous nature of the printed structure, and with image analysis software the porosity was determined to be 16.1 ± 0.4% of the total electrode volume. Gaps/voids providing a porous structure are an inherent feature found within AM devices that is highly dependent upon the ink being printed[26].

Printed CSG capacitance evaluation

The theoretical initial capacitance, C_0, and theoretical strained capacitance, were derived from previous work by Hu et al. and Kim et al., and are expressed by[4,31]

$$C_0 = pt(2l - a + 2w)\left(\frac{2n-1}{d}\right)\varepsilon_0 \quad (1)$$

$$C_{\text{perpendicular}} = pt(1-ve)((1-ve)(2l - a + 2w))\left(\frac{2n-1}{d(1+e)}\right)\varepsilon_0 \quad (2)$$

$$C_{\text{parallel}} = pt(1-ve)((1+ve)(2l - a + 2w))\left(\frac{2n-1}{d(1-e)}\right)\varepsilon_0 \quad (3)$$

where p is dielectric constant of PMMA, t is the thickness of the printed silver digit, l is the length of the digit, a is the total width of the interdigitated electrodes, w is the width of the digit, n is the number of digit pairs, d is the spacing between the digits of the electrodes, e is the strain in the sensitive axis of the strain sensor and ε_0 is the permittivity of free space. The expected change in capacitance resulting from a strain incident perpendicular and parallel to electrode orientation is depicted in Eq. 2 and Eq. 3, respectively. Briefly, when the device experiences strain perpendicular to electrode orientation the spacing between electrodes is expected to increase by a factor of $d_0(1 + e)$. However, due to Poisson contraction, it is expected that *a, w, and l* will change by a factor of (1+*ve*) from their original values, where v is the Poisson ratio of the encapsulating polymer. For the printed CSGs, the encapsulating material is PMMA with a Poisson ratio of 0.37[34]. With this phenomenon it is expected that as the PMMA is elongated in one direction it compresses in the two directions perpendicular to the direction of strain[4]. A schematic detailing the variables used in Eq. 1 and 2 is provided in Fig. 3a, and the associated dimensions are found within Fig. 3b. From the device dimensions, the initial capacitance of the printed CSGs is expected to range from 4.56 to 6.70 pF. However, the actual capacitance was measured to range between 42 pF and 15 nF. The initial capacitance values for each device can be found in Table 1., where uncertainty in C_0 and R_0 is the standard deviation in measurements. The significant deviation from theoretical capacitance is attributed to the unique geometry of the digit introduced by the printing process, which is evident in Fig. 2a–e where the electrode structure with trailing ends associated with overspray is observed in addition to a porous structure.

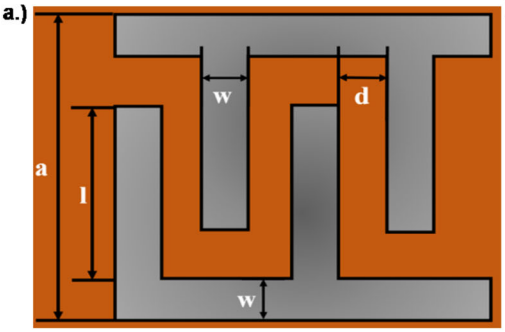

b.)

Symbol	Value
p	5.7
t	2.7±0.2 µm
w	71 ± 4 µm
l	15.74 ± 0.02 mm
d	78 ± 3 µm
a	16.07 ± 0.01 mm
n	50
ε_0	8.85418782 x 10^{-12} F/m

Fig. 3 Device design parameters for printed CSG interdigitated electrode structure. a Schematic detailing the variables to calculate theoretical capacitance, and the **b** values associated with these variables, where dimension values are reported as an average with standard deviations of measurements representative of the entire device.

Table 1. Summary of experiments.

Device	Device type	Test Type	Electrode orientation relative to strain direction	C_0 or R_0	Figure #
a	Capacitive	Dynamic, static	Perpendicular	46.436 ± 0.002 pF	4a, 4c
b	Capacitive	Dynamic, static	Perpendicular	15.22 ± 0.03 nF	4a, 4c
c	Capacitive	Dynamic, static	Perpendicular	9.25 ± 0.04 nF	4a, 4c
d	Capacitive	Dynamic, static	Parallel	42.51 ± 0.02 pF	4b, 4d
e	Capacitive	Dynamic, static	Parallel	43.61 ± 0.02 pF	4b, 4d
f	Capacitive	Cyclic	Perpendicular	11.07 ± 0.03 nF	4e
g	Capacitive	Cyclic	Perpendicular	43.57 ± 0.04 pF	4e
h	Capacitive	bending	N/A	6.22 ± 0.02 pF	4f
HBM_1	Resistive	Dynamic, Static	Perpendicular	353 Ω	5a, 5c
HBM_2	Resistive	Dynamic, Static	Perpendicular	353 Ω	5a, 5c
HBM_3	Resistive	Cyclic	Perpendicular	350 Ω	5c
HBM_4	Resistive	Cyclic	Perpendicular	350 Ω	5c

Overspray is caused by the smallest droplets within the aerosol, and can be minimized to some extent by varying the sheath, exhaust, or atomizer flow rates[35,36]. However, overspray, like void formation, is an inherent feature of aerosol jet printed devices and was found to contribute between 5 and 25 µm of additional width to the digits. Additionally, an internal capacitance may exist within the digits themselves which is associated with the structure voids themselves with air serving as the dielectric. While AJP provides significant versatility from its compatibility with a broad range of materials, consistency and reproducibility are challenges that need to be overcome. For experienced users, optimizing print parameters to mitigate these challenges can require extreme measures which include, but are not limited to, frequent replacement of ink and extensive time spent towards empirical optimization for this sensitive process[21,23,35,37,38].

CSG and RSG tensile testing

Capacitance and resistance measurements for printed CSGs and commercial RSGs, respectively, were collected for each sample prior to any load/strain being imparted to the Kevlar strap, and compared to measurements obtained before the samples were mounted into the test system to verify that no damage to the gauge had occurred during transport and setup. For each device that was tested the initial capacitance and resistance measurements can be found in Table 1. Final measurements were recorded for each sample at the conclusion of testing after the strain was released and the strap allowed to relax. However, due to the natural stretch of the Kevlar material the straps did not return to their original dimensions, and were permanently elongated after tensile loading.

Printed CSG's exhibited initial capacitance measurements that ranged from ~45 pF to ~15 nF at 10 kHz with a 5 V bias. As the observed range is significant between the printed strain gauges, representative devices from both the pF and nF regime were originally included with both perpendicular and parallel arrangement of electrodes with respect to the direction of strain. However, the device detached during dynamic testing with the representative nF device with electrodes parallel to the direction of strain.

As this work was a result of a collaboration with NASA Johnson Space Center, testing was performed in a manner that was in agreement with previously performed testing procedures[3]. The response of both capacitive and resistive devices was investigated while under dynamic, static, and cyclic loading. Mechanical testing was performed by subjecting the Kevlar webbing to targeted loading conditions rather than strain. This was the method for testing due to the fact that variations in the Kevlar webbing, attributed to the weaving process of these textiles, causes samples subjected to the same loading conditions to exhibit a different strain response between samples[32]. As the webbing is rated according to a maximum loading capacity of 26.7 kN, a peak load of 18.7 kN was selected for dynamic and static testing as it is 70% of the maximum capacity of the Kevlar webbing. Furthermore, cyclic testing was performed at targeting loads of 5.3 kN (1.2 klbf) and 10.7 kN (2.4 klbf) or 20% and 40% of maximum loading capacity of the Kevlar webbing, respectively. The targeted loads for dynamic and static testing resulted in a strain response of >5%, which still classifies the strain at which these samples were subjected to as relatively high. For reference, a summary of experiments can be found in Table 1. In addition, loading conditions were achieved with a ramp rate of 45 N s^{-1} or (10 lbf s^{-1}). Throughout dynamic testing measurements were collected at 4.4 kN (1.0 klbf), 8.9 kN (2.0 klbf), 13.3 kN (3.0 klbf), 17.8 kN (4.0 klbf) and 18.7 kN (4.2 klbf).

CSG Tensile testing results

For CSGs having electrodes arranged perpendicular to the direction of strain an inverse relationship was observed as depicted in Fig. 4a, where the MRCC (maximum relative change in capacitance) was ~20% for devices having a starting capacitance in the nF regime, and ~3% for a pF starting capacitance. This negative change in capacitance for electrodes positioned perpendicular to the direction of strain is due to the increasing elongation of the strap, which increases the distance between the electrodes resulting in a decrease to the capacitance. The indirect relationship between strain and capacitance was confirmed through 3D finite element modeling utilizing key material properties (Supplementary Fig. 1 and Table 1). However, the magnitude of relative capacitance change and corresponding gauge factor is significantly different, and that is attributed to the device features introduced from the printing process (Supplementary Fig. 2). During testing, images were captured at each change, targeted load, and/or time point. Utilizing Digimizer software, and images obtained while testing when electrodes were perpendicular to the direction of strain, the change in distance between the top of the first electrode to the bottom of the last electrode from an applied load of zero to 18.7 kN (4.20 klbF) was determined to be 815 µm. So, as the Kevlar webbing was under high load, the sensor experienced a strain of 0.037 while the webbing experienced an average strain of 0.060 ± 0.001. With that, a gauge factor of 5.2 was obtained for the perpendicular orientation with devices having a starting capacitance within the nF range. In contrast, a direct relationship between load and capacitance was observed for devices with electrodes arranged parallel to the direction of strain. As the strap is elongated, and the polyimide substrate is stretched, the spacing between the electrodes is decreased resulting in larger capacitance values. From Fig. 4b the MRCC differed by a factor of 2.3 where the MRCC for Device D was 1.6%, and for Device E was 3.7%. Dynamic testing finished immediately after a maximum load of 18.7 kN (4.2 klbF) had been reached, and static testing began. To demonstrate the printed CSGs ability to maintain a signal while under a constant load, the devices were held for a total of 65 min with measurements collected in 5 min intervals (Fig. 4c). As shown in Fig. 4c, d, while all devices were able to maintain a signal for the duration of testing, the arrangement with electrodes perpendicular to the direction of strain produced a signal having less hysteresis over the observed timeframe. Finally, cyclic testing was conducted for devices having electrodes arranged perpendicular to the direction of strain by cycling between 5.3 kN (1.2 klbf) and 10.7 kN (4.2 klbf) for a total of ten cycles (Fig. 4e).

For practical application of the printed CSG's it will be necessary to quickly and efficiently obtain the capacitance read out for analysis while minimizing the effects of interference. The ability to accommodate a large capacitance range from printed strain gauges while having a fast and efficient response can be achieved using a digital read out that uses frequency rather than voltage (See Supplementary Figs. 3–5).

RSG tensile testing results

Utilizing the same attachment strategy and testing conditions, the resistance behavior of commercially available HE-RSGs (HBM, Inc., 1-LD20-6/350) having a similar Kapton backing as the CSGs was investigated to compare and evaluate their suitability for SHM of soft structural materials. For HE-RSGs, per manufacturer instruction, the electrodes were positioned parallel to the direction of strain. The mechanism for RSG response to strain is explained with the following relationship

$$R = \frac{\rho L}{A} \tag{4}$$

where R is resistance, ρ is a material's resistivity, L is total foil

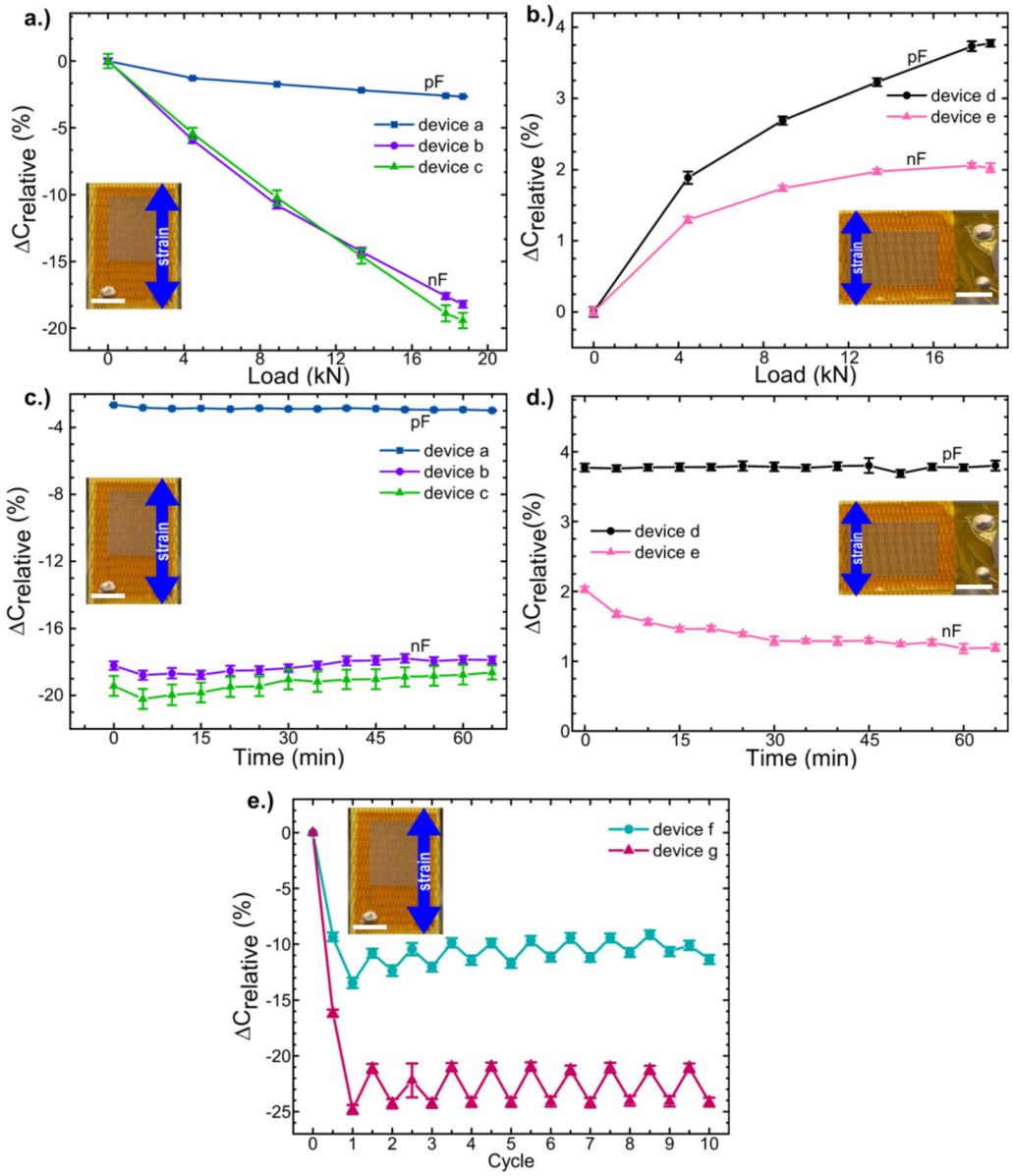

Fig. 4 Printed capacitance-based strain gauge dynamic, static and cyclic tensile testing results. Relative change in capacitance (%) for printed CSGs where a total of seven different devices (Table 1) were utilized for either dynamic (devices **a**–**e**), static (devices **a**–**e**), or cyclic (devices **f**, **g**) testing. Results for dynamic testing with a target load of 18.7 kN for devices having electrodes **a** perpendicular (devices **a**–**c**) and **b** parallel (devices d–e) to the direction of strain. Results for static testing performed at 18.7 kN for those same devices having electrodes **c** perpendicular (devices **a**–**c**) and **d** parallel (devices d-e) to the direction of strain, and **e** cyclic testing of two different devices (**f**, **g**) having electrodes perpendicular to the direction of strain. Error bars are the estimated experimental uncertainty (Supplementary Discussion). In all images, scale bars represent 1.0 cm.

length, and A is the cross-sectional area of the foil. For strain testing of these Kevlar straps, device elongation occurs with strain, and it is expected that the resistance would increase with increasing load. The response of HE-RSGs during dynamic testing is shown in Fig. 5a, where a direct relationship between resistance and load was observed up to 4.4 kN (1 klbf). While this direct relationship is expected, after the load of 4.4 kN is reached the resistance behavior transitions to an indirect relationship with the applied load at 8.9,13.3,17.8, and 18.7 kN (2, 3, 4, and 4.2 klbf, respectively). This behavior indicates that testing conditions may have caused the gauge to exceed its elongation limit, and demonstrates well-known limitations of foil based gauges for high elongation applications[39,40]. For high elongation applications where the plastic elongation conditions are met, the linearity of the strain device can vary as the gauge factor is known to modify using the guideline of $2 + \varepsilon$, where ε is the strain such that the gauge factor at a strain level of 10% is expected to be around 2.1 in tension[33,39],. Immediately after a maximum load of 18.7 kN (4.2 klbf) was achieved with dynamic testing, static testing began for period of 65 min (Fig. 5b). Another limitation is revealed during dynamic testing as signal hysteresis is shown to progress over the observed timeframe for all HE-RSG devices, which demonstrates an inability to reliably monitor strain for extended periods of time while under a constant load. Finally, HE-RSGs were subjected to cyclic testing (Fig. 5c). Cyclic testing provided further support of the aforementioned limitations of HE-RSGs as similar resistance behavior was observed after the initial target load is achieved, and signal degradation was apparent for each cycle after equilibrium had been achieved. The first cycle reveals that an equilibrium must be established prior to conducting strain measurements as

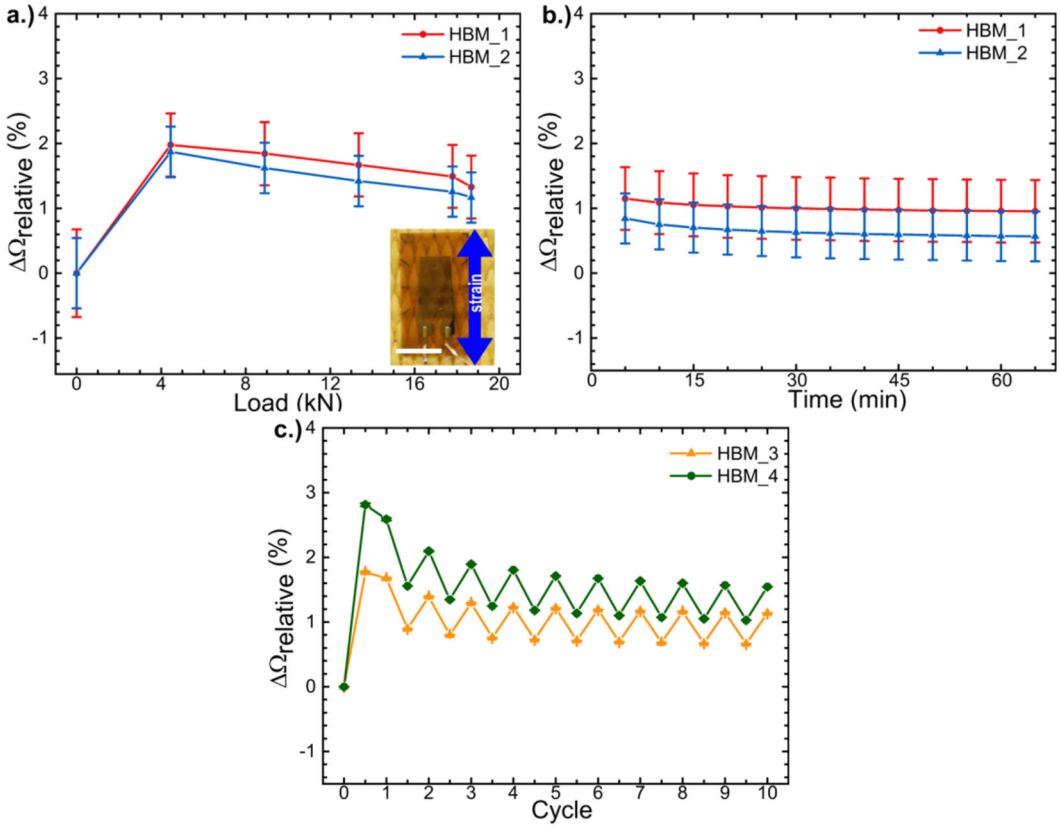

Fig. 5 Strain response for commercial resistance-based strain gauges. The strain response of commercial RSGs having their electrodes arranged parallel to the direction of strain during **a** dynamic testing with a ramp of 44.5 N/sec, **b** static testing at a load of 18.7 kN and **c** cyclic testing utilizing loads of 5.3 kN and 10.7 kN. Error bars are the estimated experimental uncertainty (Supplementary Discussion). Scale bar represents 4.0 mm.

the resistance decreases with the transition from 5.3 kN (1.2 klbf) to 10.7 kN (2.4 klbf). However, the following cycles produce the expected resistance response where an increase in resistance is observed as the applied load increases, and a decrease in resistance is observed as the applied also decreases. Notably, signal hysteresis associated with the HE-RSGs is observed for all three testing conditions and provides evidence that printed CSGs exhibit superior performance with high elongation testing conditions resulting in these devices being considered better suited for SHM for soft structural materials than HE-RSGs.

DISCUSSION

Variation in initial capacitance values, device response for the first couple of strains, etc., can be compensated for with calibration for the intended application of structural health monitoring of soft structural materials for inflatable habitats. For a crewed, inflatable space habitat, a series of strain sensors would be used in a network for structural health monitoring of the habitat. The sensors would be calibrated on the ground before launch when a precise amount of strain could be applied to the straps. Once the calibration is completed, the strain sensors would be powered off until needed again in space. After launch, deployment, and pressurization, an initial reading would be taken to get a starting strain for the strap material. This strain level would be compared to the levels recorded during the ground calibration testing to ensure no strain changes occurred during the launch phase. While the habitat will stay pressurized during its lifetime, the strain in the straps and in the gauge will change over time. This change will be tracked at regular intervals throughout the length of the mission to provide an understanding of the structural health of the habitat. Initial change during the first couple of strains can be compensated with similar calibration exercises on the ground before launch. The habitat will be testing in the space environment before it is launched and strain changes will be measured. Those strain values are expected to be representative of what would be seen during the initial change in strain once the gauges and the habitat are in space. By conducting a series of ground tests, we can fully understand and predict the behavior of the habitat and the strain measurement system and use that prediction to compensate the readings in space.

In summary, a capacitive based strain gauge was fabricated via aerosol jet printing where silver served as the capacitive material and PMMA the dielectric. Printed CSGs exhibited starting capacitance values ranging from 42 pF to 15 nF. A flexible substrate, Kapton, was employed to provide the required flexibility for these devices to withstand high load/strain, and All-purpose Barge Cement served as the adhesive between the Kapton and the Kevlar strap. Dynamic and static testing was performed for arrangements where the electrodes were oriented either perpendicular or parallel to the direction of strain, and the perpendicular arrangement was used for cyclic testing. Furthermore, HE-RSGs were tested utilizing the same attachment strategy, under the same conditions, to compare their response to printed CSGs, and to evaluate their suitability for SHM of soft structural materials. Devices having a starting capacitance in the nF range demonstrated the highest sensitivity, and a gauge factor of 5.2 was obtained for those devices having their electrodes arranged perpendicular to the direction of strain. Finally, printed CSGs were determined to be the better candidates for high elongation application as they performed better in static situations, dynamic

and cyclic events when compared to commercially available HE-RSGs.

METHODS

Device fabrication

The layout of the interdigitated CSG device is shown in Fig. 1a. Device fabrication began by depositing Sicrys™ 160PM-116 (PV Nanocell) onto a 125 µm thick DuPont™ Kapton (FPC). Printing was achieved with the pneumatic atomizer (PA) of an Optomec Aerosol Jet 200 equipped with a 200 µm nozzle. While printing, the ink was held at 23 °C to stabilize the ink, and the printed films were heated at 300 °C for 30 min. to remove any residual solvent. The tool platen temperature, nozzle diameter, and pneumatic atomizer, pneumatic exhaust and sheath gas flows were optimized to ensure the line widths and material deposition of functional materials were adequate to obtain conductive traces. Silver epoxy (Epotek, H20E) was used to adhere 30-gauge copper wire to the printed contact pads, and a layer of 950 PMMA A11 (Kayaku Advanced Materials, Inc.) was drop-coated onto the surface of the device to serve as the dielectric. Both the printed CSG and commercially acquired HE-RSG (HBM, Inc., 1-LD20-6/350) devices were attached to Kevlar straps having a maximum loading capacity of approximately 27 kN (6 klbf) with All-Purpose Barge Cement.

Characterization

Device imaging and dimensions were obtained by digital microscopy (Keyence VHX-5000), scanning electron microscopy (FEI Teneo Field Emission Scanning Electron Microscopy) and laser microscopy (Keyence VK-Z260K 3D Laser Scanning Confocol Microscope). Additional height profiles were obtained with a Bruker Dektak XT-A Stylus Profilometer fitted with a 2 µm stylus. A Leica EM UC6 microtome equipped with glass blades was used to produce CSG cross-sections. Furthermore, cross-sectioning required devices to first be encapsulated in Quickstick 135 mounting wax (Scanning Microscopy Services) prior to slicing. CSG cross-sections were carbon-coated to prevent charging of the specimen.

Device attachment

Strain gauges were attached to Kevlar webbing (1991-25.4 mm, Type VI, Class 9) nominally rated at 26.7 kN (6 klbf), and manufactured to Mil-T 87130 manufacturing specifications. Attaching the gauges to the Kevlar webbing was accomplished with a contact cement known as APBC (All-Purpose Barge Cement; Barge Cements, Inc.). This cement is a polychloroprene based adhesive that is well known for its high strength and flexibility and is typically used in the leather, shoe and prosthetic industries. While the tensile modulus for APBC is not reported or available, polychloroprene is reported to have a tensile modulus of 21 MPa[41]. This is well below the tensile modulus for Kapton and Kevlar, which indicates that it is well-suited for the intended application. For testing purposes, multiple adhesives were considered including Double/Bubble epoxy, Pliobond 25, DAP Cove Base Zocalo construction adhesive, and GE silicone II caulk. However, APBC was the only adhesive capable of maintaining the integrity of the bond while under high strain such as that produced while testing Kevlar straps. Adhering the printed CSGs and RSGs to the Kevlar strap began by applying a thin layer of APBC to both the testing strap and the backside of the printed CSG or RSG. The two items were immediately bonded together with the adhesive sandwiched between the CSG or RSG backing and the strap. The bond was cured for 24 hours.

Testing

After the bond was fully cured the Kevlar straps were attached to the webbing grips on the MTS test system by wrapping each end of the strap at least three times around the grip to ensure the strap would not come loose during testing. The grips were positioned such that there was ~24 inches between the base of each grip with the strain gauge positioned in the center. Samples tested included gauges mounted with electrodes both perpendicular and parallel to the direction of strain resulting in positive and negative changes in capacitance, respectively. The leads to the LCR meter were attached and supported to ensure the leads would not come into contact with each other, would not place undue tension on the copper wire attachments, and would remain relatively stable during testing. CSG devices were attached both perpendicular and parallel to the direction of strain while RSG devices were only tested having electrodes parallel to the direction of strain, and both types of devices were attached to Kevlar straps with All-Purpose Barge Cement. Strain testing was performed with an MTS 810 Material Test System equipped with a 100 kN load head, ADMET GRW-50T (Part No. 3218-00225) webbing grips, and FlexTest SE Station Manager software. Capacitance measurements were obtained with an Agilent HP 4284A Precision LCR Meter (10 kHz at 5 V), and resistance measurements were obtained with a Keithley 2182A/6220 (−1 to 1 mA), Printed CSG and commercial RSG devices were studied under dynamic, cyclic, and static loads while Kevlar straps were subjected to a maximum load of 18.7 kN (4.2 klbf) during static and dynamic loads at a ramp rate of 45 N s^{-1} (10 lbf s^{-1}). During dynamic testing capacitance measurements were obtained every 4.5 kN (1 klbf) up to the maximum load of 18.7 kN (4.2 klbf), and static loads were held for a total of one hour ten minutes with capacitance measurements taken every five minutes. Additionally, printed CSGs and commercial RSGs were characterized under cyclic loading of 5.3 kN (1.2 klbf) and 10.7 kN (2.4 klbf) for ten total cycles with a ramp rate of 89 N s^{-1} (20 lbf s^{-1}) with capacitance measurements taken at 90 s intervals between each cycle. Macro images of the CSGs were taken in tandem with capacitance measurements in order to determine the gauge factor for the CSGs. Images were recorded with a Canon EOS 70D digital SLR camera outfitted with a Tamron AF 90 mm f/2.8 1:1 macro lens. The camera was held stationary on a tripod and a remote trigger was used to eliminate vibration during image exposure. The ruler imaged next to the CSG during testing was kept in-plane with the device for use in measuring the dimensional change experienced by the CSG at strain. Gauge factor calculations were completed using values for the dimensional changes obtained in conjunction with digital imaging processing software.

DATA AVAILABILITY

The data that supports the findings of this study are available from the authors on reasonable request, see author contributions for specific data sets.

CODE AVAILABILITY

The code that supports the findings of this study are available from the authors on reasonable request, see author contributions for specific data sets.

Received: 8 November 2019; Accepted: 11 October 2020;
Published online: 23 November 2020

REFERENCES

1. NASA Scientific and Technical Information Program. *Intelligent Flexible Materials for Space Structures*. Technical Report No. NASA/CR–2010-216682 (2010).
2. Li, J., Longtin, J. P., Tankiewicz, S., Gouldstone, A. & Sampath, S. Interdigital capacitive strain gauges fabricated by direct-write thermal spray and ultrafast laser micromachining. *Sens. Actuator A Phys.* **133**, 1–8 (2007).
3. Litteken, D. Evaluation of strain measurement devices for inflatable structures. *AIAA*. **58**, 0426. https://doi.org/10.2514/6.2017-0426. (2017).
4. Kim, S. R., Kim, J. H. & Park, J. W. Wearable and transparent capacitive strain sensor with high sensitivity based on patterned Ag nanowire networks. *ACS Appl. Mater. Interfaces* **9**, 26407–26416 (2017).
5. Cohen, D. J., Mitra, D., Peterson, K. & Maharbiz, M. M. A highly elastic, capacitive strain gauge based on percolating nanotube networks. *Nano Lett.* **12**, 1821–1825 (2012).
6. Amjadi, M., Pichitpajongkit, A., Lee, S., Ryu, S. & Park, I. Highly stretchable and sensitive strain sensor based on silver nanowire-elastomer nanocomposite. *ACS Nano* **8**, 5154–5163 (2014).
7. Andeen, C., Fontanella, J. & Schuele, D. A capacitive gauge for the accurate measurement of high pressures. *Rev. Sci. Instrum.* **42**, 495–496 (1971).
8. Amjadi, M., Kyung, K. U., Park, I. & Sitti, M. Stretchable, skin-mountable, and wearable strain sensors and their potential applications: a review. *Adv. Funct. Mater.* **26**, 1678–1698 (2016).
9. Lipomi, D. J. et al. Skin-like pressure and strain sensors based on transparent elastic films of carbon nanotubes. *Nat. Nanotechnol.* **6**, 788–792 (2011).
10. Tsouti, V., Mitrakos, V., Broutas, P. & Chatzandroulis, S. Modeling and development of a flexible carbon black-based capacitive strain sensor. *IEEE Sens. J.* **16**, 3059–3067 (2016).
11. Matsuzaki, R. & Todoroki, A. Wireless flexible capacitive sensor based on ultra-flexible epoxy resin for strain measurement of automobile tires. *Sens. Actuator A Phys.* **140**, 32–42 (2007).

12. Glass, S. W., Fifield, L. S., Sriraman, A. & Bowler, N. Inter-digital capacitive sensor for evaluating cable insulation through jacket and aging. *19th EnvDeg, Proc.* **2102**, 020024 (2019)
13. Zeiser, R., Fellner, T. & Wilde, J. Capacitive strain gauges on flexible polymer substrates for wireless, intelligent systems. *J. Sens. Sens. Syst.* **3**, 77–86 (2014).
14. Lynch, J. P. A summary review of wireless sensors and sensor networks for structural health monitoring. *Struct. Health Monit.* **38**, 91–128 (2006).
15. Cao, C., Andrews, J. B. & Franklin, A. D. Completely printed, flexible, stable, and hysteresis-free carbon nanotube thin-film transistors via aerosol jet printing. *Adv. Electron. Mater.* **3**, 1700057 (2017).
16. Cheng, M. Y., Lin, C. L., Lai, Y. T. & Yang, Y. J. A polymer-based capacitive sensing array for normal and shear force measurement. *Sensors* **10**, 10211–10225 (2010).
17. Wang, F. X. et al. Aerosol-jet printing of nanowire networks of zinc octaethylporphyrin and its application in flexible photodetectors. *Chem. Commun.* **49**, 2433–2435 (2013).
18. Obata, K. et al. Hybrid 2D patterning using UV laser direct writing and aerosol jet printing of UV curable polydimethylsiloxane. *Appl. Phys. Lett.* **111**, 121903 (2017).
19. Feng, J. Q. & Renn, M. J. Aerosol Jet ® direct-write for microscale additive manufacturing. *J. Micro Nanomanuf.* **7**, 011004 (2019).
20. Wilkinson, N. J., Smith, M. A. A., Kay, R. W. & Harris, R. A. A review of aerosol jet printing—a non-traditional hybrid process for micro-manufacturing. *Int. J. Adv. Manuf. Technol.* https://doi.org/10.1007/s00170-019-03438-2 (2019).
21. Secor, E. B. Principles of aerosol jet printing. *Flex. Print. Electron.* **3**, 035002 (2018).
22. Folgar, C. E., Suchicital, C. & Priya, S. Solution-based aerosol deposition process for synthesis of multilayer structures. *Mater. Lett.* **65**, 1302–1307 (2011).
23. Mahajan, A., Frisbie, C. D. & Francis, L. F. Optimization of aerosol jet printing for high-resolution, high-aspect ratio silver lines. *ACS Appl. Mater. Interfaces* **5**, 4856–4864 (2013).
24. Paulsen, J. A., Renn, M., Christenson, K. & Plourde, R. Printing conformal electronics on 3D structures with aerosol jet technology. *2012 Future of Instrumentation International Workshop - IEEE-FIIW, Proc.* **2012**, 47–50. https://doi.org/10.1109/FIIW.2012.6378343. (2012).
25. Hedges, M., Borras, A. & Services, M. N. 3D Aerosol Jet ® Printing-Adding Electronics Functionality to RP/RM. *2012 DDMC Conference, Proc.* **2012**, 1–5 (2012).
26. Pandhi, T. et al. Electrical transport and power dissipation in aerosol-jet-printed graphene interconnects. *Sci. Rep.* **8**, 1–10 (2018).
27. Deiner, L. J. & Reitz, T. L. Inkjet and aerosol jet printing of electrochemical devices for energy conversion and storage. *Adv. Eng. Mater.* **19**, 1600878 (2017).
28. Madou, M. J. Chemical, Photochemical, and Electrochemical Forming Techniques. in *Manufacturing Techniques for Microfabrication and Nanotechnology*, 509–567 (CRC Press, 2011).
29. Morales-Rodriguez, M. E., Joshi, P. C., Humphries, J. R., Fuhr, P. L. & McIntyre, T. J. Fabrication of low cost surface acoustic wave sensors using direct printing by aerosol inkjet. *IEEE Access* **6**, 20907–20915 (2018).
30. Sethumadhavan, V., Saraf, S. & Chaudhari, A. Development of printable electronic materials for low cost flexible sensor fabrication. *2017 IEEE - ICEICE, Proc.* **2017**, 1–5. https://doi.org/10.1109/ICEICE.2017.8192449. (2017).
31. Hu, C. F., Wang, J. Y., Liu, Y. C., Tsai, M. H. & Fang, W. Development of 3D carbon nanotube interdigitated finger electrodes on polymer substrate for flexible capacitive sensor application. *Nanotechnology* **24**, 1–14 (2013).
32. Selig, M. M. et al. Creep burst testing of a woven inflatable module. *2nd AIAA Spacecraft Structures Conference, Proc.* **2015**, 1625. https://doi.org/10.2514/6.2015-1625 (2015).
33. Rahman, M. T., Rahimi, A., Gupta, S. & Panat, R. Microscale additive manufacturing and modeling of interdigitated capacitive touch sensors. *Sens. Actuator A Phys.* **248**, 94–103 (2016).
34. MatWeb. Overview of materials for acrylic, general purpose, molded. http://www.matweb.com/search/DataSheet.aspx?MatGUID=3cb08da2a0054447a3790015b7214d07&ckck=1. (2020)
35. Chen, G., Gu, Y., Tsang, H., Hines, D. R. & Das, S. The effect of droplet sizes on overspray in aerosol-jet printing. *Adv. Eng. Mater.* **20**, 1701084 (2018).
36. Verheecke, W. et al. Aerosol jet® printing of silver interconnects on polyimide film for embedded electronics applications. *8th International DAAAM Baltic Conference, Proc.* **8**, 19–21 (2012).
37. Salary, R. (Ross) et al. Computational fluid dynamics modeling and online monitoring of aerosol jet printing process. *J. Manuf. Sci. Eng.* **139**, 021015 (2016).
38. Gu, Y., Gutierrez, D., Das, S. & Hines, D. R. Inkwells for on-demand deposition rate measurement in aerosol-jet based 3D printing. *J. Micromech. Microeng.* **27**, 097001 (2017).
39. VPG. High-Elongation Strain Measurements Tech-Tip TT-605. *Micro-Measurements* ***11085****, 1–4*. http://www.vishaypg.com/doc?11085 (2015).
40. HBM Test and Measurement. Strain gauges: First Choice for Strain Measurements, Catalogue. *Hottinger Baldwin Messtechnik GmbH* **2008**, 321–328 (2008).
41. Ames Industrial. Polychloroprene Rubber - neoprene datasheet. *Ames Rubber Manufacturing* http://www.amesrubberonline.com/pdf/polychloroprene-neoprene.pdf. (2020).

ACKNOWLEDGEMENTS

This material is based upon work supported under an Integrated University Program Graduate Fellowship, and was supported in part by Department of Energy In-Pile Instrumentation program under DOE Idaho Operations Office Contract DE-AC07-05ID14517 and by the National Aeronautics Space Administration under award #80NSSC18M0088. The views and opinions of authors expressed herein do not necessarily state or reflect those of the U.S. Government or any agency thereof. D.E. also acknowledges career development support by Institutional Development Awards (IDeA) from the National Institute of General Medical Sciences of the National Institutes of Health under Grants #P20GM103408 and P20GM109095.

AUTHOR CONTRIBUTIONS

K.F. designed and printed the test structures, performed SEM cross-section imaging and analysis, and performed uncertainty analysis calculations. J.W., K.F., D.L. and D.E. conceived of the experimental design and together with B.J., supervised the experiments. K.F., J.W., and T.P. performed the mechanical testing of all strain gauges. K.T. performed laser microscope imaging and profilometry analysis. T.B. and Z.D. performed finite element and analytical modeling analysis. Finally, K.L.R. and B.C.J. designed and tested the frequency based digital readout. All authors contributed to the development of the paper.

COMPETING INTERESTS

The authors declare no competing interests.

ADDITIONAL INFORMATION

Supplementary information is available for this paper at https://doi.org/10.1038/s41528-020-00095-4.

Correspondence and requests for materials should be addressed to D.E.

Reprints and permission information is available at http://www.nature.com/reprints

Publisher's note Springer Nature remains neutral with regard to jurisdictional claims in published maps and institutional affiliations.